Journal of Alloys and Compounds 921 (2022) 166124

Contents lists available at ScienceDirect

Journal of Alloys and Compounds

journal homepage: www.elsevier.com/locate/jalcom

Phase diagram of the Cu–Ni_3Al pseudo-binary system

Satoshi Semboshi[a,b,*], Toshiki Anno[b], Yasuyuki Kaneno[b]

[a] Institute for Materials Research, Tohoku University, Katahira 2-1-1, Aoba-ku, Sendai, Miyagi 980-8577, Japan
[b] Department of Materials Science, Osaka Prefecture University, Gakuen-cho 1-1, Naka-ku, Sakai, Osaka 599-8531, Japan

ARTICLE INFO

Article history:
Received 5 April 2022
Received in revised form 31 May 2022
Accepted 30 June 2022
Available online 7 July 2022

Keywords:
Cu
Ni_3Al
Phase diagram
Eutectic reaction
Microstructure

ABSTRACT

Cu–Ni–Al alloys with a Ni to Al ratio of approximately 3.0 are of particular interest for the development of electrically conductive products; thus, investigating their phase behavior is essential for achieving specific properties in these materials. In this study, the phase diagram of the Cu–Ni_3Al pseudo-binary system was experimentally determined using cast and fully heat-treated Cu–Ni_3Al alloys with a wide range of compositions, via microstructural observation and different quantitative analyses. The Cu–Ni_3Al system undergoes a eutectic reaction Liquid ↔ α-Cu solid solution (Cu_{ss}) with an FCC structure +γ′-Ni_3Al with an ordered FCC $L1_2$ structure. As the combined Ni and Al (Ni_3Al) content increased, the microstructure transitioned from a single α-Cu_{ss} phase to two eutectic phases (α-Cu_{ss} and γ′-Ni_3Al), to a primary γ′-Ni_3Al phase and two eutectic phases, and to a single γ′-Ni_3Al phase. The solidus and liquidus temperatures increased with the (Ni+Al) content. The solid solubility of (Ni+Al) in the α-Cu_{ss} phase ($C_{(Ni+Al)}$) could be described by an Arrhenius-type equation ($\ln C_{(Ni+Al)} = 5.50 - 2637/T$), indicating a significant temperature dependence. In contrast, the solubility of Cu in the γ′-Ni_3Al phase did not significantly decrease with the temperature. The phase diagram of the Cu–Ni_3Al system was constructed from these results. The phase diagram will be useful in the development of Cu–Ni–Al alloys with exceptional strength and electrical conductivity.

1. Introduction

The Cu–Ni–Al ternary system involves materials of academic and practical relevance, such as Al- and Cu-based alloys for functional structure materials [1–4], shape memory Cu–Al and Ni–Al alloys [5–7], intermetallic compounds Ni_3Al and NiAl as strengthening phases in high temperature structural materials [8–11], and Cu–-Ni–Al-based high entropy alloys [12,13]. Cu-based alloys that have been proposed for structural and electrical applications include not only Cu solid solution alloys, but also age-hardenable systems, in which, some precipitates, such as NiAl and Ni_3Al intermetallic compounds, are formed in the Cu matrix [14–18]. Miyamoto et al. studied the hardness of Cu–Ni–Al alloys within a wide Cu-rich range using a diffusion coupling method [19,20]. They found that the alloys with compositions along the Cu–Ni_3Al segment in an isothermal Cu–Ni–Al phase diagram exhibited better mechanical strength than those with other compositions. Recently, Semboshi et al. [21] demonstrated that a Cu–20 at% Ni–6.7 at% Al alloy solid solution treated at 1000 °C and then aged at 600 °C possessed exceptional strength, with Vickers hardness > 340 HV, tensile strength of approximately 1000 MPa, and a good electrical conductivity of 8 % IACS. Notably, its strength is the highest among commercial Cu-based alloys without any additional deformation strain. The superior strength of the Cu–Ni–Al alloys is due to high-density fine Ni_3Al precipitates formed coherently with the Cu matrices [17–21].

As previously described, the Cu–Ni–Al alloys with a Ni to Al ratio of approximately 3.0 have good mechanical strength and are especially relevant for the development of electrically conductive products. In this context, the Cu–Ni_3Al pseudo-binary phase diagram, which graphically represents the phases in equilibrium for two components of Cu and Ni_3Al (although it consists of three components: Cu, Ni, and Al) at different temperatures, would be useful for controlling the microstructure and properties by adjusting the alloy composition and heat treatment conditions. However, the equilibrium data of the Cu–Ni_3Al phase diagram have not been precisely evaluated because of insufficient experimental information, except for several isothermal Cu–Ni–Al ternary phase diagrams that have been published [22–27]. Although the phase diagram of Cu–Ni_3Al system can be calculated with data from the reported thermodynamic databases, as shown in Fig. 1, they remain inconsistent with the actual alloy microstructure [21]. Therefore, further experimental studies are needed to assess the database for the Cu–Ni_3Al alloy

* Corresponding author at: Institute for Materials Research, Tohoku University, Katahira 2-1-1, Aoba-ku, Sendai, Miyagi 980-8577, Japan.
E-mail addresses: semboshi@imr.tohoku.ac.jp (S. Semboshi), anknown.glayer@outlook.jp (T. Anno), kaneno@mtr.osakafu-u.ac.jp (Y. Kaneno).

https://doi.org/10.1016/j.jallcom.2022.166124
0925-8388/

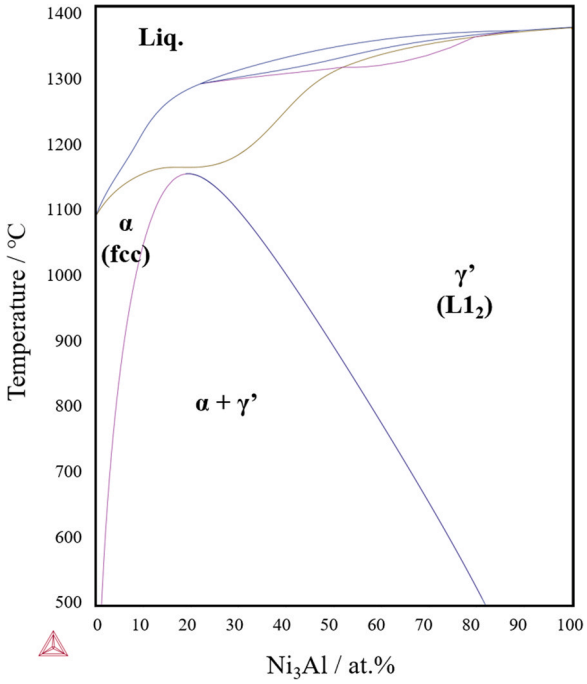

Fig. 1. A phase diagram of the Cu–Ni_3Al pseudo-binary system calculated using the software Thermo-calc2021a. The α and γ′ denote Cu solid solution with a disordered FCC structure and Ni_3Al with an ordered FCC one ($L1_2$), respectively. The details of the calculation are provided in the Supplementary material.

system. The objective of this study is to experimentally determine the phase diagram of Cu–Ni_3Al system. For this purpose, several fully heat-treated Cu-Ni_3Al alloys were prepared and analyzed using conventional microstructural observation and various quantitative analyses.

2. Materials and methods

The seventeen Cu–Ni_3Al alloys with a nominal Ni_3Al content ranging from 26.7 to 94 at% were fabricated as follows; the raw materials (99.99 % copper, 99.99 % nickel, and 99.99 % aluminum) obtained from High Purity Materials Laboratory Co., LTD., Japan, were melted with a high-frequency induction-heating apparatus in an argon atmosphere, followed by casting into a copper mold. In this procedure, bullet-shaped alloy ingots 15 mm in diameter and 50–60 mm in length were obtained. The contaminated surface layer was removed by mechanical machining, and the ingots were sliced into disk-shaped samples with a diameter of 10 mm and thickness of 2.0 mm. The samples were placed inside quartz tubes, where the atmosphere was replaced with high-purity argon. The samples were heat-treated at temperatures in the range of 800–1250 °C for 24 h or 48 h to achieve equilibrium, and were then water quenched. Here, the heat treatment period for equilibration was reported to be less than 1 h at 750 °C for the Cu–26.7 at% Ni_3Al alloy [21]. It was also confirmed that the difference between the weighting composition before casting and the composition after final heat treatment for equilibration, which were chemically analyzed using an inductively coupled plasma optical emission spectrometer, was within 0.4 at% for all the prepared specimens.

In addition, Cu–2.67 at% Ni_3Al alloy sheet with a thickness of 0.3 mm was obtained from DOWA METALTECH Co., Ltd., Japan. The alloy sheet was fabricated via melt casting, hot-rolling, cold-rolling, and solid-solution treatment at 1000 °C for 2 h, followed by quenching in water. The details of the fabrication procedure of the sheet are described in a previous paper [21]. The strip-like

Table 1
List of the Cu-Ni_3Al alloys prepared in this study. The alloys, having a disk-shape and measuring 10 mm in diameter and 2.0 mm in thickness or a strip with dimensions of 60 mm × 7 mm × 0.3 mm, were heat-treated for equilibrium and subjected to analysis to identify the equilibrium phase as listed. In this study, DSC measurements were also carried out for the seventeen specimens of Cu–(26.7, 32, 35, 40, 45, 50, 55, 58, 60, 62, 65, 70, 75, 80, 86, 90, and 94) at% Ni_3Al alloys.

Composition of prepared alloys (at% Ni_3Al)	Final heat treatment conditions for equilibration			Equilibrium phases		Analyzed method
	Temp. (°C)	Time (h)	Disk/Strip	Phase 1	Phase 2	
26.7	1050	24	Disk	α-Cu_{ss}		FESEM, TEM
	1000	24	Strip	α-Cu_{ss}		FESEM, TEM
	750	~ 1	Strip	α-Cu_{ss}	γ′-Ni_3Al	Electrical resistivity
	650	~ 680	Strip	α-Cu_{ss}	γ′-Ni_3Al	Electrical resistivity
	600	~ 1440	Strip	α-Cu_{ss}	γ′-Ni_3Al	Electrical resistivity
	550	~ 840	Strip	α-Cu_{ss}	γ′-Ni_3Al	Electrical resistivity
32	1050	24	Disk	α-Cu_{ss}		FESEM, TEM
35	1050	24	Disk	α-Cu_{ss}	γ′-Ni_3Al	FESEM, TEM
	900	48	Disk	α-Cu_{ss}	γ′-Ni_3Al	TEM-EDS
	850	48	Disk	α-Cu_{ss}	γ′-Ni_3Al	TEM-EDS
	800	48	Disk	α-Cu_{ss}	γ′-Ni_3Al	TEM-EDS
40	1150	24	Disk	α-Cu_{ss}	γ′-Ni_3Al	FESEM, TEM
	1050	24	Disk	α-Cu_{ss}	γ′-Ni_3Al	FESEM, TEM
50	1150	24	Disk	α-Cu_{ss}	γ′-Ni_3Al	FESEM, TEM
	1050	24	Disk	α-Cu_{ss}	γ′-Ni_3Al	FESEM, TEM
60	1150	24	Disk	α-Cu_{ss}	γ′-Ni_3Al	FESEM, TEM
	1050	24	Disk	α-Cu_{ss}	γ′-Ni_3Al	FESEM, TEM
70	1200	24	Disk	α-Cu_{ss}	γ′-Ni_3Al	FESEM, TEM
	1150	24	Disk	α-Cu_{ss}	γ′-Ni_3Al	FESEM, TEM
	1050	24	Disk	α-Cu_{ss}	γ′-Ni_3Al	FESEM, TEM
80	1250	24	Disk	α-Cu_{ss}	γ′-Ni_3Al	FESEM, TEM
	1200	24	Disk	α-Cu_{ss}	γ′-Ni_3Al	FESEM, TEM
	1150	24	Disk	α-Cu_{ss}	γ′-Ni_3Al	FESEM, TEM
	1050	24	Disk	α-Cu_{ss}	γ′-Ni_3Al	FESEM, TEM
86	1250	24	Disk	γ′-Ni_3Al		FESEM, TEM
	1150	24	Disk	α-Cu_{ss}	γ′-Ni_3Al	FESEM, TEM
90	1050	24	Disk	γ′-Ni_3Al		FESEM, TEM
	950	48	Disk	γ′-Ni_3Al		TEM-EDS
	850	48	Disk	α-Cu_{ss}	γ′-Ni_3Al	TEM-EDS
	800	48	Disk	α-Cu_{ss}	γ′-Ni_3Al	TEM-EDS

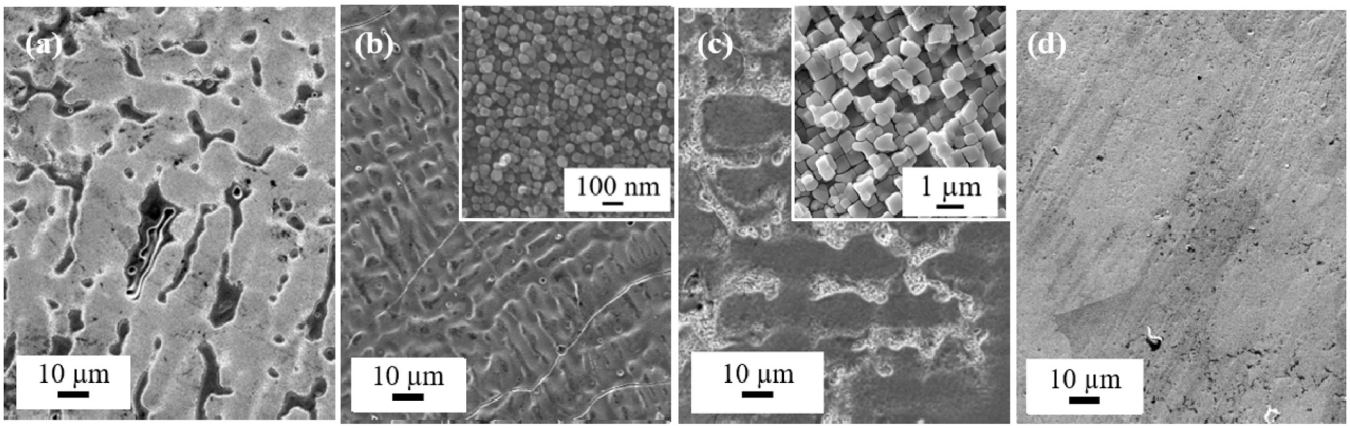

Fig. 2. Field emission scanning electron microscopy micrographs for the following as-cast alloys: Cu–32 at% Ni_3Al (a), Cu–40 at% Ni_3Al (b), Cu–80 at% Ni_3Al (c), and Cu–94 at% Ni_3Al (d). The insets in (b) and (c) are magnified images of each corresponding material.

specimens with dimensions of 60 mm × 7 mm × 0.3 mm were cut out from the sheet using a shearing machine. These specimens were isothermally heat-treated at temperatures of 550–750 °C for 0.5 min–1440 h and then quenched into water. The heat treatment conditions for the alloys prepared in this study are summarized in Table 1.

The microstructure of the prepared alloys was studied using field emission scanning electron microscopy (FESEM, JSM-7001F JEOL, Japan), with an accelerating voltage of 15 keV, and transmission electron microscopy (TEM, JEM-2000EXII JEOL, Japan, and 002B Topcon, Japan) with an accelerating voltage of 200 keV coupled with energy dispersive X-ray spectroscopy (EDS, Noran system 7 ThermoFisher, Japan). For the FESEM observation, the disk-shaped samples measuring 10 mm in diameter and 2.0 mm in thickness were mechanically polished with a 1500-grade emery paper and mirror-polished by buffing with a fine Al_2O_3 slurry. To obtain a sound surface for FESEM observation, the Cu-rich alloy samples (Cu–(26.7–60) at% Ni_3Al) were then electrochemically etched using an aqueous solution of 40 % phosphoric acid at 20 °C and a direct voltage of 2.0 V. In contrast, the Ni_3Al-rich alloy samples (Cu–(62–94) at% Ni_3Al) were electrochemically etched using a methanol solution of 15 % nitric acid at 20 °C and a direct voltage of 20 V. For the TEM observation, the disk-shaped specimens were mechanically polished down to a thickness of under 30 μm. The polished foils were fixed with a single-hole molybdenum mesh measuring 0.8 mm and 3.0 mm in inner and outer diameter, respectively; they were then subjected to a low-angle ion milling apparatus (PIPS2, JEOL, Japan) with argon ion at an accelerating voltage of 3.0 keV and irradiating angle of 10°. The composition of each alloy in a local area was determined by averaging at least five TEM–EDS measurements. The minimum local area detected for the EDS measurements in this study was approximately 100 nm in diameter (which corresponds to the minimum diameter of the focused electron beam in the TEM apparatus).

To study the phase transitions and determine the solidus and liquidus temperatures, differential scanning calorimetry (DSC) measurements using DSC 404 C Netzsch Japan were performed. For DSC measurement, a disk-shaped specimen measuring 3.0 mm in diameter and 20 mm in thickness (weighing approximately 400 mg) was cut out via electrical discharge machining. The damaged surface was then mechanically polished using emery paper. During the DSC measurement, the disk alloy was put in a Al_2O_3 crucible under a continuous flow of argon (99.99999 % purity). The rate of heating was fixed at 10 °C/min after instrument calibration. The solidus and liquidus temperatures were determined from the onset of the peak and from the peak maximum, respectively, on the heating curve, ignoring the heat rate dependency [31,32]. The details of the DCS analysis are provided in the Supplementary Material.

To estimate the composition of the matrix phase in each alloy, the electrical resistivity of the Cu–2.67 at% Ni_3Al alloy specimens (60 mm × 7 mm × 0.3 mm) was measured using the direct current four-probe method at 20 °C and a current of 100 mA [28].

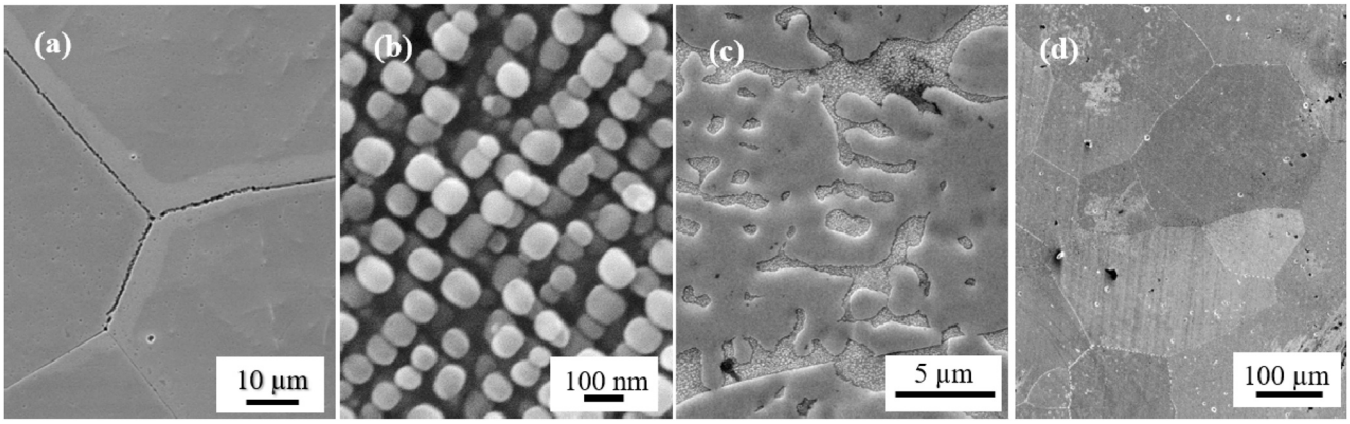

Fig. 3. Field emission scanning electron microscopy micrographs for the following alloys heat-treated at 1050 °C for 24 h: Cu–32 at% Ni_3Al (a), Cu–40 at% Ni_3Al (b), Cu–80 at% Ni_3Al (c), and Cu–90 at% Ni_3Al (d).

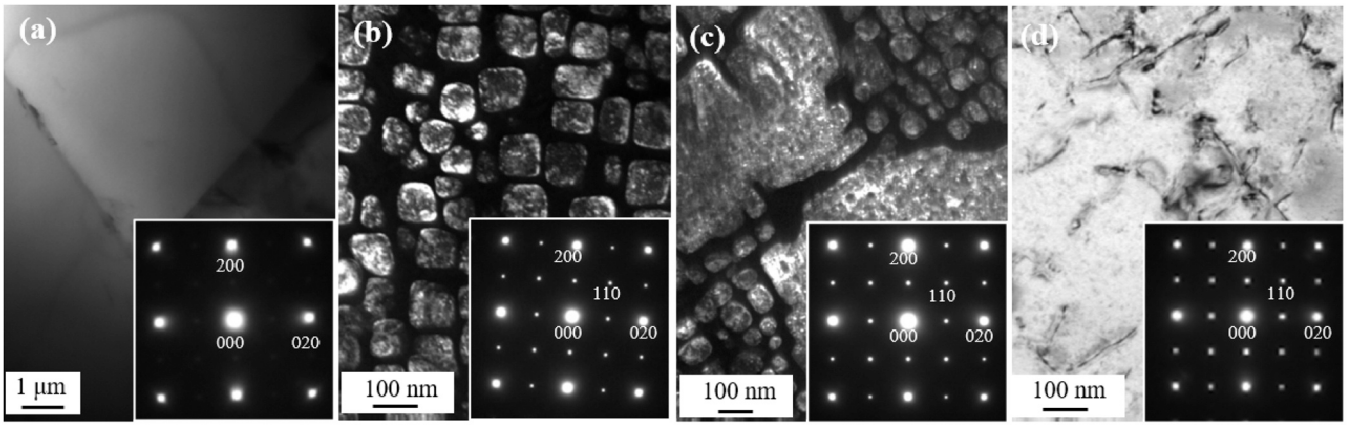

Fig. 4. Transmission electron microscopy micrograph and selected area diffraction pattern (inset), for the following alloys heat-treated at 1050 °C for 24 h: Cu–32 at% Ni_3Al (a), Cu–40 at% Ni_3Al (b), Cu–80 at% Ni_3Al (c), and Cu–90 at% Ni_3Al (d). (a) and (d) are the bright-field images. Some dislocations were observed in a parent grain in (d). (b) and (c) are dark-field images obtained from an ordered lattice diffraction spot of $110_{\gamma'}$. The direction of the incident beam was 001_{α} (or $001_{\gamma'}$).

3. Results and discussion

3.1. Constituent phases

Fig. 2 shows FESEM images of the as-cast Cu–(32, 40, 80, 94) at% Ni_3Al alloys (hereafter, the unit "at%" will be omitted). The Cu–(26.7–32) Ni_3Al alloys cast into copper mold showed a single phase of typical dendritic morphology, as shown in Fig. 2(a) for the Cu–32 Ni_3Al alloy [29]. The microstructure of the cast Cu–(35 and 40) Ni_3Al alloys appeared dendritic at low magnification, similar to that of the Cu–32 Ni_3Al alloys (Fig. 2(a)); however, at high magnification, two phases with fine spherical particles in the matrix in the inter-dendritic region were evident (see the inset in Fig. 2(b)). Primary dendrites consisting of a single phase and an inter-dendritic region containing fine spherical particles in the matrix were observed in the cast Cu–(45–90) Ni_3Al alloys (Fig. 2(c)). This was similar to the microstructure of the Cu–40 Ni_3Al alloys shown in Fig. 2(b). The cast Cu–94 Ni_3Al alloys showed a typical single-phase morphology (Fig. 2(d)).

Fig. 3 shows FESEM images for the Cu–(32, 40, 80, 90) Ni_3Al alloys heat-treated at 1050 °C for 24 h. The single-phase morphology of the Cu–(26.7–32) Ni_3Al alloys transitioned from dendrites to equiaxied grains through the heat treatment, as shown in Fig. 3(a). In the heat-treated Cu–(35 and 40) Ni_3Al alloys, spherical particles with a size of approximately 100 nm were dispersed in the matrix (Fig. 3(b)). The size of spherical particles was larger than that of the corresponding as-cast alloy (see the inset in Fig. 2(b)). In the heat-treated Cu–(45–86) Ni_3Al alloys, primary dendrites and an inter-dendritic region containing coarsened spherical particles in the matrix were observed (Fig. 3(c)). The Cu–90 Ni_3Al alloy exhibited a single-phase morphology with equiaxied grains (Fig. 3(d)), which transitioned from the dendritic and inter-dendritic microstructure as shown in Fig. 2(c).

To identify the constituent phases, TEM observation was carried out. Fig. 4 shows a dark field (DF) image together with the corresponding selected area electron diffraction (SAED) pattern (in the inset) for the Cu–(32, 40, 80, 90) Ni_3Al alloy heat-treated at 1050 °C for 24 h. The SAED pattern obtained for a grain in the Cu–(26.7–32) Ni_3Al alloy could be indexed as an α-Cu solid solution (α-Cu_{ss}) with an FCC structure (Strukturbericht symbol: A1, space group: *F*m_3m, lattice parameter: a = 0.361 nm), as shown in Fig. 4(a). This indicates that the Cu–(26.7–32) Ni_3Al alloys had a single phase of α-Cu_{ss}. However, for the Cu–(35–40) Ni_3Al alloys, the SAED pattern exhibits the fundamental lattice diffraction spots from an α-Cu_{ss} phase as well as the ordered lattice diffraction spots from a γ'-Ni_3Al intermetallic compound with an ordered FCC structure ($L1_2$, *P*m_3m, a = 0.358 nm) [30]. In the DF image, obtained from an ordered lattice diffraction spot of $110_{\gamma'}$, spherical particles with an average diameter of approximately 100 nm appear dispersed homogeneously in the matrix. Consequently, the spherical particles shown in Fig. 3(b) and Fig. 4(b) were identified as γ'-Ni_3Al. Moreover, the fine spherical particles were coherently formed with a preferential crystal orientation relationship with the α-Cu_{ss} matrix of $<100>_{\alpha}$ // $<100>_{\gamma'}$ and $\{001\}_{\alpha}$ // $\{001\}_{\gamma'}$, that is, the so-called "cube-on-cube" relationship [21].

Based on the analogous TEM observations and SAED analyses, it can be suggested that the Cu–(45–86) Ni_3Al alloys comprised primary dendrites of γ'-Ni_3Al and inter-dendritic regions of γ'-Ni_3Al particles in an α-Cu_{ss} matrix, as shown in Fig. 4(c), and the Cu–(90–94) Ni_3Al alloys had a single phase of γ'-Ni_3Al, as shown in Fig. 4(d). Moreover, the microstructures of all the Cu–Ni_3Al alloys fully heat-treated at temperatures between 550 and 1250 °C exhibited no other constituent phase besides α-Cu_{ss} and γ'-Ni_3Al.

3.2. Solidus and liquidus temperatures

Fig. 5 shows the DSC heating curves for the Cu–(32, 70, and 94) Ni_3Al alloys (the DSC curves for the other Cu–Ni_3Al alloys are shown in Fig. S1 in the Supplementary Material). An endothermic peak attributed to melting was observed in each curve at > 1150 °C. The solidus and liquidus temperatures (T_S and T_L respectively) were obtained from the peaks at the positions marked with solid triangles in Fig. 5 [31,32]. Both the T_S and T_L increased as the combined content of Ni and Al (Ni+Al) in the Cu–Ni_3Al alloys increased. Additionally, inflection points (T_i) observed in the curves for the Cu–(45–70) Ni_3Al alloys (marked with an open triangle in Fig. 5(b)) were associated with the eutectic reaction *Liq.* ⇔ α-Cu_{ss} + γ'-Ni_3Al between the T_S and T_L, as will be discussed later.

3.3. Solubility lines

3.3.1. α-Cu_{ss} side

Based on the FESEM and TEM images, the Cu–26.7 Ni_3Al alloys heat-treated at 1050 and 1000 °C for 24 h had a single phase of α-Cu_{ss}. In contrast, when these alloys were heat-treated again at temperatures between 550 and 750 °C, high density γ'-Ni_3Al particles precipitated in the α-Cu_{ss} matrix, as previously reported [21].

Fig. 6(a) shows the electrical resistivity of the Cu–26.7 Ni_3Al alloys heat-treated at 1000 °C for 24 h and then at temperatures between 550 and 750 °C. The resistivity values for all the alloys heat-treated at 1000 °C were approximately 345 nΩ·m, and decreased at an early stage of the additional heat treatment, eventually stabilizing

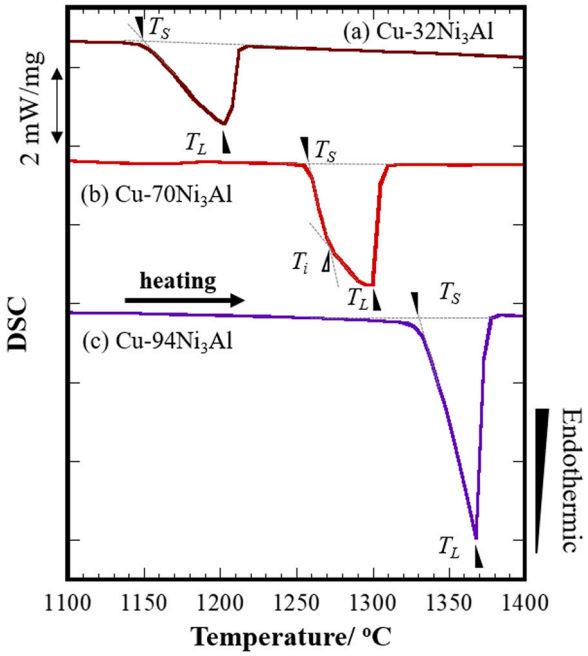

Fig. 5. Differential scanning calorimetry curves for the following alloys: Cu–32 at% Ni_3Al (a), Cu–70 at% Ni_3Al (b), and Cu–94 at% Ni_3Al (c), measured at a heating rate of 10 °C/min in a 50 mL/min flow of pure argon.

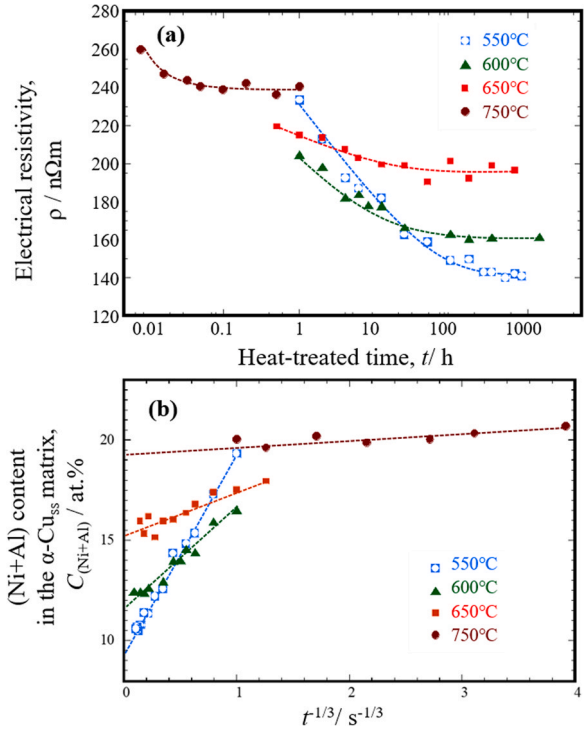

Fig. 6. (a) Electrical resistivity of the Cu–26.7 at% Ni_3Al alloys heat-treated at 1000 °C for 24 h and then heat-treated again at temperatures between 550 and 750 °C. (b) Changes in the content of solute (Ni+Al) in the α-Cu solid solution matrix over time in the latter heat treatment, estimated from the electrical resistivity values shown in (a).

at different values. This decrease in the resistivity of the heat-treated alloys suggests that the content of the solute (Ni+Al) in the α-Cu_{ss} matrix decreased as the γ'-Ni_3Al particles precipitated. Additionally, the stabilization of the electrical resistivity suggests that the composition distribution of the constituent phases was close to equilibrium [21,33], although the fine γ'-Ni_3Al precipitates continued to grow with a slight compositional distribution so as to reduce the interfacial energy of fine particle, that is, Ostwald ripening [34].

The content of the solute (Ni+Al) in the α-Cu_{ss} matrix ($C_{(Ni+Al)}$), can be estimated from the data of electrical resistivity of the alloys (ρ). Here, we assumed that the value of ρ for the heat-treated Cu–26.7 Ni_3Al alloys was primarily given by that of the α-Cu_{ss} matrix (ρ_α), ignoring the contribution of the γ'-Ni_3Al precipitates (The validity of this assumption will be discussed later in this section). Thus, the value of ρ_α [Ω·m] is given by the individual contents of Ni and Al in the α-Cu_{ss} matrix, C_{Ni} and C_{Al}, according to Nordheim's equation [35]:

$$\rho \approx \rho_\alpha = \rho_{Cu} + C_{Ni}\Delta\rho_{Ni}(100 - \Lambda_{Ni}C_{Ni})/100 + C_{Al}\Delta\rho_{Al}(100 - \Lambda_{Al}C_{Al})/100 \quad (1)$$

In Eq. (1), ρ_{Cu} is the electrical resistivity of pure Cu (17.24 nΩ·m), $\Delta\rho_{Ni}$ and $\Delta\rho_{Al}$ are coefficients with reported values of 12.2 and 12.5 nΩ·m/at% respectively, and Λ_{Ni} and Λ_{Al} are correction coefficients, with values of 0.3 and 4.5 respectively [36]. Considering that the ratio of C_{Ni}/C_{Al} is always 3.0 even after the heat treatment, $C_{(Ni+Al)}$ can be calculated from the data shown in Fig. 6(a) and Eq. (1). The calculated values are plotted in Fig. 6(b).

It should be noted that some material distribution must occur between the α-Cu_{ss} matrix and the γ'-Ni_3Al precipitates during the additional heat treatment due to the Ostwald ripening, as can be explained by the Gibbs–Thompson effect [34]. According to the theory by Kuehmann and Voorhees [37], the variation in the phase composition as a function of the heat treatment time (t) is described by the following equation, where $C_{(Ni+Al),e}$ is the equilibrium solubility of the solute (Ni+Al) in the α-Cu_{ss} matrix and k is a constant representing the kinetics:

$$C_{(Ni+Al)} - C_{(Ni+Al),e} = k\, t^{-1/3} \quad (2)$$

At heat treatment at temperatures between 550 and 750 °C, the data of $C_{(Ni+Al)}$ as a function of t are well fitted with Eq. (2), as shown in Fig. 6(b). Thus, when $t^{-1/3}\rightarrow 0$ ($t\rightarrow\infty$), the values of $C_{(Ni+Al),e}$ calculated with Eq. (2) are 9.4, 11.7, 15.2, and 19.1 at% at 550, 600, 650, and 750 °C, respectively.

According to the Cu–Ni–Al isothermal phase diagrams previously reported [22–27], the volume fractions of γ'-Ni_3Al in the Cu–26.7 Ni_3Al alloys fully heat-treated at temperatures above 550 °C would be lower than 15 vol %. Therefore, the error caused by neglecting the contribution of the γ'-Ni_3Al precipitates in the calculation of $C_{(Ni+Al),e}$ from the electrical resistivity measurements would be of 1.5 at% toward the Cu-poor side, at most.

The Cu–35 Ni_3Al alloys that were heat-treated at 1050 °C for 24 h and then heat-treaded again at 800, 850, and 900 °C for 48 h exhibited two-phase microstructures of γ'-Ni_3Al precipitates of particles larger than 100 nm in the α-Cu_{ss} matrix, as representatively shown in Fig. 7(a). The compositions of the α-Cu_{ss} matrix and γ'-Ni_3Al precipitates for the alloy heat-treated at 850 °C were plotted in the Gibbs triangle of Fig. 7(b). As the two phases in the Cu–35 Ni_3Al alloy were assumed to be in equilibrium at 850 °C, the line segment connecting their compositions corresponds to the tie-line, where the alloy composition of Cu–35 Ni_3Al is found (solid line in Fig. 7(b)). The composition of the α-Cu_{ss} matrix phase measured by TEM–EDS is very close to the Cu–Ni_3Al line (dotted line). Therefore, this composition can be roughly regarded as the equilibrium solubility of the solute (Ni+Al) in the α-Cu_{ss} matrix ($C_{(Ni+Al),e}$) for the phase diagram of the Cu–Ni_3Al pseudo-binary system. For the alloy heat-treated at 800 and 900 °C, the same consideration can be made. Notably, the $C_{(Ni+Al),e}$ determined from TEM–EDS measurements should be slightly higher than the strictly equilibrium composition because of the Gibbs–Thompson effect caused by extremely small particle sizes of γ'-Ni_3Al precipitates (100–150 nm) [34].

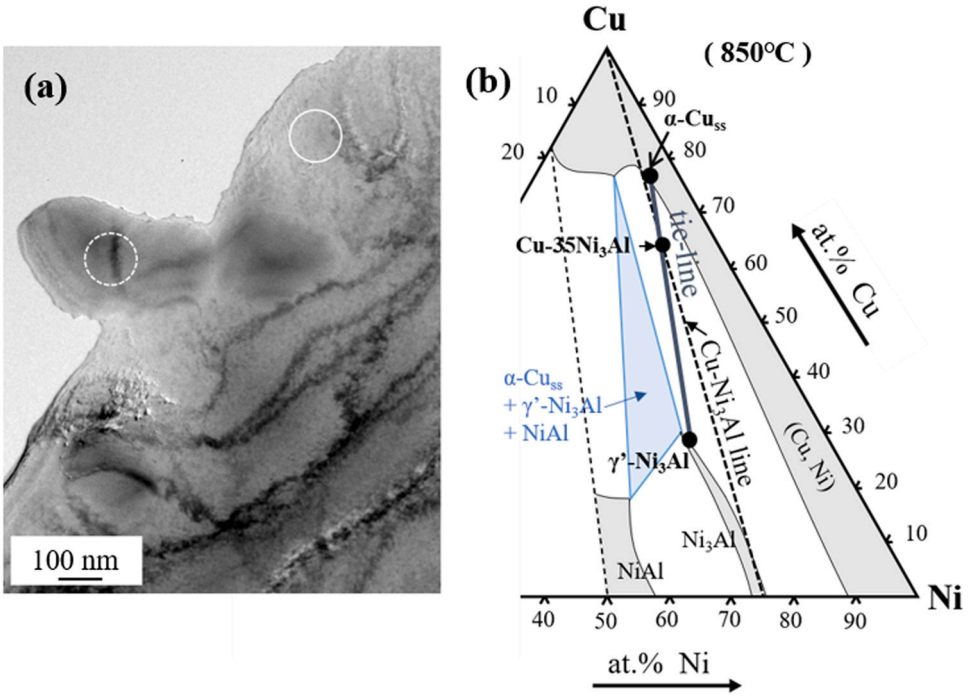

Fig. 7. (a) Transmission electron microscopy bright field micrograph for the Cu–35 at% Ni_3Al alloy heat-treated at 1050 °C for 24 h and then heat-treated again at 850 °C for 48 h. The compositions of the α-Cu solid solution matrix and γ'-Ni_3Al particles, as indicated by solid and dotted circles in (a), respectively, were measured using transmission electron microscopy coupled with energy-dispersive X-ray spectroscopy, and plotted in the Gibbs triangle in (b). (b) Partial isothermal phase diagram at 850 °C predicted from the phase diagram at 800 °C [23].

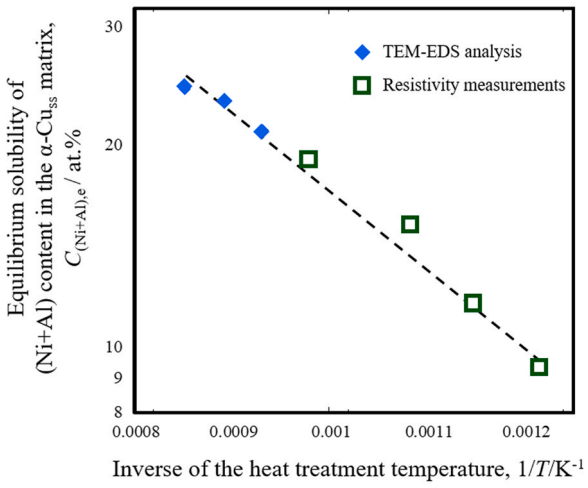

Fig. 8. Arrhenius plot of the equilibrium solubility of solute (Ni+Al) in the α-Cu solid solution matrix, estimated from the measurements of electrical conductivity shown in Fig. 6, and from the transmission electron microscopy coupled with energy-dispersive X-ray spectroscopy analyses.

Fig. 8 shows the temperature dependence of $C_{(Ni+Al),e}$, which was obtained from the electrical resistivity and TEM–EDS measurements. The values of ln $C_{(Ni+Al),e}$ can be linearly fitted against the reciprocal of the absolute temperature T [K], resulting in the following equation:

$$\ln C_{(Ni+Al),e} = 5{\cdot}50 - 2637/T \quad (3)$$

This equation would represent the solubility of (Ni+Al) in the α-Cu_{ss}, when some assumptions and approximations are incorporated to obtain the $C_{(Ni+Al),e}$ from the electrical resistivity and TEM–EDS measurements.

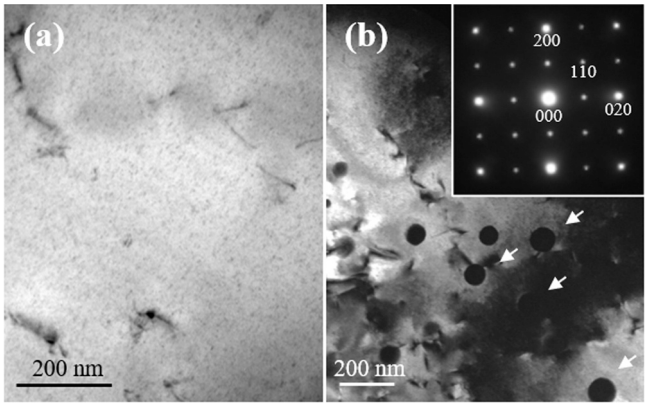

Fig. 9. Transmission electron microscopy micrographs and selected area diffraction pattern (inset in (b)), for the Cu–90 at% Ni_3Al alloy heat-treated at 1050 °C for 24 h and then heat-treated again for 48 h at 950 °C (a) and 900 °C (b). The dark field image in (b) was obtained from an ordered lattice diffraction spot of $110_{\gamma'}$. The dark spherical contrasts marked with white arrows correspond to α-Cu solid solution particles.

3.3.2. *γ′-Ni₃Al side*

The Cu–90 Ni_3Al alloy heat-treated at 1050 °C for 24 h contained a single phase of γ'-Ni_3Al, as shown in Fig. 3(d). This was also the case after the additional heat treatment at 950 °C for 48 h, as shown in Fig. 9(a). In contrast, spherical α-Cu_{ss} particles precipitated in the γ'-Ni_3Al matrix in the alloys that underwent additional heat treatment at temperatures below 900 °C (Fig. 9(b)). This indicates that the solvus temperature between the single-phase region of γ'-Ni_3Al and the two-phase region of α-Cu_{ss} and γ'-Ni_3Al is between 900 and 950 °C. Similarly, from the microstructure of the Cu–86 Ni_3Al alloy it can be deduced that the solvus temperature is between 1150 and 1250 °C.

The Cu content of the γ'-Ni_3Al matrix region without α-Cu_{ss} particles was measured by TEM–EDS for the Cu–90 Ni_3Al alloys heat-treated at 1050 °C for 24 h and then again at 800, 850, and 900 °C for

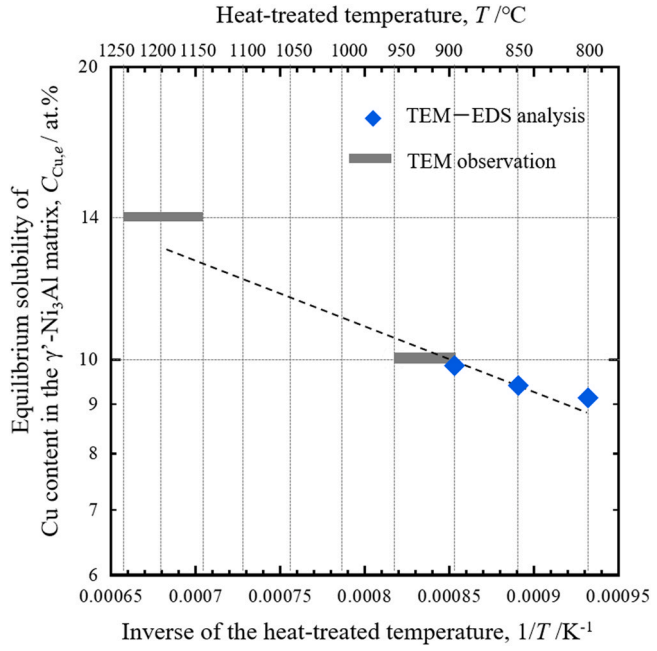

Fig. 10. Arrhenius plot of the equilibrium solubility of solute Cu in the γ-Ni_3Al matrix, estimated from the transmission electron microscopy (TEM) microstructural observations and TEM coupled with energy-dispersive X-ray spectroscopy analyses.

48 h. The obtained values were 9.1, 9.4, and 9.9 at%, respectively. These values might be slightly higher than that of the strictly equilibrium composition due to the Gibbs–Thompson effect caused by the extremely small article size of α-Cu_{ss} precipitates (approximately 150 nm, as shown in Fig. 9). Thus, the solubility of Cu in the γ′-Ni_3Al matrix (C_{Cu}) can be approximated by the solid line in Fig. 10 obtained from the microstructural observation and TEM–EDS measurements, although it is difficult to formulate the temperature dependence of C_{Cu} in a manner similar to Eq. (3) because of lacking in the quantitative data at high temperatures. Note that it was hard to determine the Cu solute content in the γ′-Ni_3Al matrix using electrical resistivity, as it was done for the (Ni+Al) solute in the α-Cu_{ss} matrix (see Section 2.3.1), because of limited information on the parameters for Nordheim's equation (Eq. (1)) [38].

3.4. Phase diagram of the Cu–Ni_3Al pseudo-binary system

As a summary of the results in the previous sections, we proposed a phase diagram of the Cu–Ni_3Al system, which is shown in Fig. 11. The crystal structures of the solid phase that were observed in the Cu–Ni_3Al system are listed in Table 2.

The liquidus and solidus lines are drawn using the data obtained from the DSC measurements shown in Fig. 5 and Fig. S1 in the Supplementary Material, as well as the data for pure copper (melting point: 1086 °C) and stoichiometric binary Ni_3Al (melting point 1380 °C) [39]. Note that the T_S and T_L values measured by the DCS should have some deviation at least ± 3 °C, which was from experimental accuracy and heating rate dependency (see Supplementary material). Both the T_S and T_L monotonically increased as the (Ni+Al) content in the Cu–Ni_3Al alloys increased.

A two-phase microstructure with a primary dendritic γ′-Ni_3Al structure and an inter-dendritic region of α-Cu_{ss} and γ′-Ni_3Al was observed in the cast Cu–(40–80) Ni_3Al alloys (see Fig. 2(c)). Additionally, the T_i was detected in the endothermic peak in the DSC curves (Fig. 5(b) and Fig. S1 in the Supplementary Material). This suggests that the eutectic reaction of *Liq.* → α-Cu_{ss} + γ′-Ni_3Al occurred at T_i during the solidification process. When the melts of the Cu–(40–80) Ni_3Al alloys are cooled, first, the primary γ′-Ni_3Al is formed below the T_L (*Liq.* → *Liq.* + γ′-Ni_3Al), and then, the remaining liquid phase decomposes into α-Cu_{ss} and γ′-Ni_3Al via a eutectic reaction. The reaction progresses in the region of coexistence of the three phases (liquid, α-Cu_{ss}, and γ′-Ni_3Al), as shown in Fig. 11. The expanded three-phase coexistence region is not strange, because the Cu–Ni_3Al pseudo-binary system is essentially a ternary system of Cu, Ni, and Al, and the three-phase equilibrium region does not contradict the Gibbs phase rule.

The eutectic microstructure of the Cu–Ni_3Al system exhibited spherical or near-cuboidal γ′-Ni_3Al particles homogeneously dispersed in the α-Cu_{ss} matrix. The microstructure was different from the lamellar and fibrous microstructures often observed in conventional eutectic alloys [40]. This can be explained by the low-energy coherent interfaces on all sides of the γ′-Ni_3Al particles, because γ′-

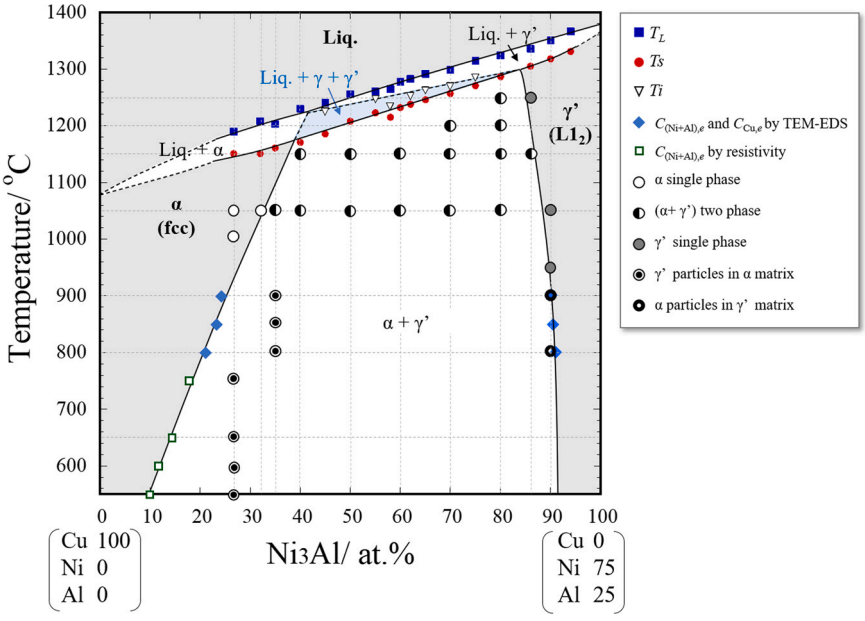

Fig. 11. Phase diagram for the Cu–Ni_3Al pseudo-binary system proposed in this study.

Table 2
Crystal structure data for Cu-Ni_3Al pseudo-binary system.

Phase	Composition, at% Ni_3Al	Phase symbol	Space group	Struktur-bericht designation	Prototype
(α-Cu)	0 to ~ 38	*cF4*	$Fm\bar{3}m$	A1	Cu
(γ′-Ni_3Al)	~84–100	*cF4*	$Pm\bar{3}m$	$L1_2$	$AuCu_3$

Ni_3Al has the same FCC-based crystal structure and a similar lattice parameter to the parent α-Cu_{ss}. Thus, when the mismatch between the α-Cu_{ss} and γ′-Ni_3Al is small, the shape of the coherent particles must be spherical to minimize the interfaces.

Because the phase diagram of the Cu–Ni_3Al system is classified as a eutectic type, the microstructure for the heat-treated Cu–Ni_3Al alloys mainly transitioned in the following order as the (Ni+Al) content increased (Figs. 3 and 4): a single α-Cu_{ss} phase, two eutectic phases (α-Cu_{ss} and γ′-Ni_3Al), a primary γ′-Ni_3Al and two eutectic phases, and a single γ′-Ni_3Al phase. The solubility curve of (Ni+Al) in α-Cu_{ss} and that of Cu in γ′-Ni_3Al were drawn with the results and data obtained using Eq. (3) in Fig. 8 and Fig. 10, as show in Fig. 11. The solubility of Cu in the γ′-Ni_3Al phase was estimated to reach a maximum of approximately 15 at% at temperatures close to 1300 °C, and did not significantly decrease with the decrease in temperature. In contrast, the solubility of (Ni+Al) in the α-Cu_{ss} phase, as described by Eq. (3), exhibits a relatively strong temperature dependence. This could be favorable for age-hardening alloys; it makes it possible to control the amount of precipitate and the alloy strength broadly by choosing the composition and aging temperature, because of the wide range of supersaturation and supercooling conditions that can be applied. In particular, the fine and hard γ′-Ni_3Al particles precipitate coherently with the α-Cu_{ss} matrix, which would lead to effective age-hardening. As previously mentioned, there is already evidence of aged Cu–Ni–Al alloys with good strength and electrical conductivity [21]. The phase diagram proposed in this study will be useful for the future development of such alloys.

4. Conclusions

A reliable Cu–Ni_3Al pseudo-binary phase diagram is required for the development of electrically conductive products to control the microstructures and mechanical properties by adjusting the alloy composition and heat-treatment conditions. In this study, we gathered experimental data from qualitative microstructural observation and quantitative analyses (thermal analysis, electrical resistivity measurements, and TEM–EDS measurements) of the constituent phases to construct a Cu–Ni_3Al pseudo-binary phase diagram. The results obtained are described next.

(1) Only two solid phases, α-Cu_{ss} and γ′-Ni_3Al, were observed in the Cu–(26.7–94) at% Ni_3Al alloys cast and heat-treated at temperatures between 550 and 1250 °C. As the (Ni+Al) content increased, the alloy structure changed from a single α-Cu_{ss} phase to two eutectic phases, then to a primary γ′-Ni_3Al phase and two eutectic phases, and finally to a single γ′-Ni_3Al phase. The eutectic microstructure of the Cu–Ni_3Al alloy system contained spherical γ′-Ni_3Al particles coherent with the α-Cu_{ss} matrix.
(2) The solidus and liquidus temperatures of the Cu–Ni_3Al alloys monotonically increased from 1084° to 1380°C as the (Ni+Al) content increased. The solid solubility of (Ni+Al) in the α-Cu_{ss} phase $C_{(Ni+Al)}$ could be accurately described with the following Arrhenius-type equation: $\ln C_{(Ni+Al)} = 5.50 - 2637/T$, ($T$: absolute temperature). The solubility of Cu in γ′-Ni_3Al phase was estimated to reach a maximum of approximately 15 at%, and did not significantly decrease with the temperature.
(3) A phase diagram of Cu–Ni_3Al system was constructed. The phase diagram is classified as a eutectic type, and has a coexistence region of three phases (liquid, α-Cu_{ss}, and γ′-Ni_3Al).

The phase diagram constructed in this study will be useful for the future development of aged Cu–Ni–Al alloys with good strength and electrical conductivity.

Funding sources

This work was supported by a cooperative program of the Collaborative Research and Development Center for Advanced Materials (CRDAM) in IMR of Tohoku University (Grant No. 202011-CRKEQ-0404), the Japan Society for the Promotion of Science (Grant-in-Aid for Scientific Research (B) No. 18H01743), and the Japan Copper and Brass Association.

CRediT authorship contribution statement

S. Semboshi: Conceptualization, Methodology, Sample preparation, Formal analysis, Validation, Writing – review & editing, Project administration, Funding acquisition, Supervision. **T. Anno**: Investigation, Formal analysis, Data curation, Writing – original draft. **Y. Kaneno**: Conceptualization, Resource, Validation, Supervision.

Declaration of Competing Interest

The authors declare that they have no known competing financial interests or personal relationships that could have appeared to influence the work reported in this paper.

Acknowledgements

The authors thank Prof. R. Kainuma and Prof. T. Omori of Tohoku University for their useful input. The authors also thank Mr. E. Aoyagi, and Ms. M. Tateishi of the Institute for Materials Research (IMR) of Tohoku University for their experimental assistance. Finally, the authors thank Dr. H. Hyodo and Mr. T. Shuto of DOWA METALTECH Co., LTD. for the preparation of the samples.

Appendix A. Supporting information

Supplementary data associated with this article can be found in the online version at doi:10.1016/j.jallcom.2022.166124.

References

[1] K.G. Watkins, M.A. McMahon, W.M. Steen, Microstructure and corrosion properties of laser surface processed aluminium alloys: a review, Mater. Sci. Eng. A 231 (1997) 55–61, https://doi.org/10.1016/S0921-5093(97)00034-8
[2] J.H. Kim, J.H. Jeun, H.J. Chun, Y.R. Lee, J.T. Yoo, J.H. Yoon, H.S. Lee, Effect of precipitates on mechanical properties of AA2195, J. Alloy. Compd. 669 (2016) 187–198, https://doi.org/10.1016/j.jallcom.2016.01.229
[3] B. Schönfeld, H. Roelofs, A. Malik, G. Kostorz, J. Plessing, H. Neuhäuser, The microstructure of Cu-Al, Acta Mater. 44 (1996) 335–342, https://doi.org/10.1016/1359-6454(95)00164-9
[4] N. Rajasekaran, S. Mohan, Structure, microstructure and corrosion properties of brush-plated Cu–Ni alloy, J. Appl. Electrochem. 39 (2009) 1911–1916, https://doi.org/10.1007/s10800-009-9899-x

[5] N. Zárubová, A. Gemperle, V. Novák, Initial stages of γ_2 precipitation in an aged Cu-Al-Ni shape memory alloy, Mater. Sci. Eng. A 222 (1997) 166–174, https://doi.org/10.1016/S0921-5093(96)10520-7
[6] Y.D. Kim, C.M. Wayman, Shape recovery and phase transformation behavior in Ni–Al alloys, Metall. Trans. A 23 (1992) 2981–2986, https://doi.org/10.1007/BF02646116
[7] A. Agrawal, R.K. Dube, Methods of fabricating Cu-Al-Ni shape memory alloys, J. Alloy. Compd. 750 (2018) 235–247, https://doi.org/10.1016/j.jallcom.2018.03.390
[8] R.D. Noebe, R.R. Bowman, M.V. Nathal, Physical and mechanical properties of the B2 compound NiAl, Int. Mater. Rev. 38 (1993) 193–232, https://doi.org/10.1179/imr.1993.38.4.193
[9] I. Celikyyuek, N.O. Korpe, T. Olcer, R. Gurler, Microstructure, properties and wear behaviors of $(Ni_3Al)_p$ reinforced Cu matrix composites, J. Mater. Sci. Technol. 27 (2011) 937–943, https://doi.org/10.1016/S1005-0302(11)60167-9
[10] S. Semboshi, H. Tsuda, Y. Kaneno, A. Iwase, T. Takasugi, Thermal conductivity of Ni3V–Ni3Al pseudo-binary alloys, Intermetallics 59, 2015, pp. 1–7. ⟨https://doi.org/10.1016/j.intermet.2014.12.006⟩.
[11] J. Wu, C. Li, Y. Liu, Y. Wu, Q. Guo, H. Li, H. Wang, Effect of annealing treatment on microstructure evolution and creep behavior of a multiphase Ni_3Al-based superalloy, Mater. Sci. Eng. A 743 (2019) 623–635, https://doi.org/10.1016/j.msea.2018.11.126
[12] A.I. Yurkova, V.V. Cherniavsky, V. Bolbut, M. Krüger, I. Bogomol, Structure formation and mechanical properties of the high-entropy AlCuNiFeCr alloy prepared by mechanical alloying and spark plasma sintering, J. Alloy. Compd. 786 (2019) 139–148, https://doi.org/10.1016/j.jallcom.2019.01.341
[13] A.M. Manzoni, H.M. Daoud, R. Voelkl, U. Glatzel, N. Wanderka, Influence of W, Mo and Ti trace elements on the phase separation in Al8Co17Cr17Cu8Fe17Ni33 based high entropy alloy, Ultramicroscopy 159 (2015) 265–271, https://doi.org/10.1016/j.ultramic.2015.06.009
[14] Y.R. Cho, Y.-H. Kim, T.D. Lee, Precipitation hardening and recrystallization in Cu-4 % to 7 % Ni-3 % Al alloys, J. Mater. Sci. 26 (1991) 2879–2886, https://doi.org/10.1007/BF01124816
[15] Z. Sierpiński, J. Gryziecki, Phase transformations and strengthening during ageing of CuNi10Al3 alloy, Mater. Sci. Eng. A 264 (1999) 279–285, https://doi.org/10.1016/S0921-5093(98)01083-1
[16] C.H. Chen, C.C. Yang, T.F. Liu, Phase transition in a Cu–14.1Al–9.0Ni alloy, Mater. Sci. Eng. A 354 (2003) 377–386, https://doi.org/10.1016/S0921-5093(03)00041-8
[17] K.A. Christofidou, K.J. Robinson, P.M. Mignanelli, Ed.J. Pickering, N.G. Jones, H.J. Stone, The effect of heat treatment on precipitation in the Cu-Ni-Al alloy Hiduron® 130, Mater. Sci. Eng. A 692 (2017), pp. 192–198, https://doi.org/10.1016/j.msea.2017.03.069
[18] K. Ishida, Alloy design and development of advanced materials based on phase diagrams and microstructural control, Mater. Trans. 61 (2020) 807–819, https://doi.org/10.2320/matertrans.MT-M2019362
[19] T. Miyamoto, M. Nagasako, T. Omori, K. Ishida, R. Kainuma, Characterization of mechanical and electrical properties in Cu-Ni-Al alloys using combinatorial method, J. Jpn. Inst. Copp. 54 (2015) 190–195.
[20] K. Ishida, Alloy design and development of advanced materials based on phase diagrams and microstructural control, Mater. Trans. 61 (2020) 807–819.
[21] S. Semboshi, R. Hariki, T. Shuto, H. Hyodo, Y. Kaneno, N. Masahashi, Age-induced precipitating and strengthening behaviors in a Cu–Ni–Al alloy, Metall. Mater. Trans. A 52 (2021) 4934–4945.
[22] A. Prince, G. Effenberg, G. Petzow, F. Aldinger, P. Rogl, L. Rokhlin (Eds.), Ternary Alloys: A Comprehensive Compendium of Evaluated Constitutional Data and Phase Diagrams, MSlGmbH, Stuttgart,Germany, 1991.
[23] C.H. Wang, S.W. Chen, C.H. Chang, J.C. Wu, Phase equilibria of the ternary Cu-Ni-Al system and interfacial reactions of related systems at 800 °C, Metall. Mater. Trans. A 34 (2003) 199–209, https://doi.org/10.1007/s11661-003-0322-7
[24] R. Kainuma, X.J. Liu, I. Ohnuma, S.M. Hao, K. Ishida, Miscibility gap of B2 phase in NiAl to Cu_3Al section of the Cu–Al–Ni system, Intermetallics 13 (2005) 655–661, https://doi.org/10.1016/j.intermet.2004.10.005
[25] J. Kundin, P. Wang, H. Emmerich, R. Schmid-Fetzer, Investigation of Cu-Ni-Al alloy solidification: Thermodynamics, experiments and phase-field modeling, Eur. Phys. J. Spec. Top. 223 (2014) 567–590, https://doi.org/10.1140/epjst/e2014-02110-6
[26] W. Wang, H.L. Chen, H. Larsson, H. Mao, Thermodynamic constitution of the Al–Cu–Ni system modeled by CALPHAD and ab initio methodology for designing high entropy alloys, Calphad 65 (2019) 346–369, https://doi.org/10.1016/j.calphad.2019.03.011
[27] Z.M. Li, X.N. Li, Y.L. Hu, Y.H. Zheng, M. Yang, N.J. Li, L.X. Bi, R.W. Liu, Q. Wang, C. Dong, Y.X. Jiang, X.W. Zhang, Cuboidal γ' phase coherent precipitation-strengthened Cu–Ni–Al alloys with high softening temperature, Acta Mater. 203 (2021) 116458, https://doi.org/10.1016/j.actamat.2020.10.076
[28] S. Semboshi, Y. Kaneno, T. Takasugi, N. Masahashi, High strength and high electrical conductivity Cu-Ti alloy wires fabricated by aging and severe drawing, Metall. Mater. Trans. A 49 (2018) 4956–4965, https://doi.org/10.1007/s11661-018-4816-8
[29] R.C. Reed, Superalloys, Cambridge University Press, 2006.
[30] Y. Mishima, S. Ochiai, T. Suzuki, Lattice parameters of Ni(γ), Ni_3Al(γ') and Ni_3Ga (γ') solid solutions with additions of transition and B-subgroup elements, Acta Met. 33 (1985) 1161–1169, https://doi.org/10.1016/0001-6160(85)90211-1
[31] K. Han, I. Ohnuma, R. Kainuma, Experimental determination of phase equilibria of Al-rich portion in the AleFe binary system, J. Alloy. Compd. 668 (2016) 97–106.
[32] T. Zienert, O. Fabrichnaya, Experimental investigation and thermodynamic assessment of the Al-Fe system, J. Alloy. Compd. 743 (2018) 795–811.
[33] S. Semboshi, S. Amano, J. Fu, A. Iwase, T. Takasugi, Kinetics and equilibrium of age-induced precipitation in Cu-4 At. PctTi binary alloys, Metall. Mater. Trans. A 48 (2017) 1501–1511, https://doi.org/10.1007/s11661-016-3949-x
[34] H.A. Calderon, P.W. Voorhees, J.L. Murray, G. Kostorz, Ostwald ripening in concentrated alloys, Acta Metal. Mater 42 (1994) 991–1000.
[35] L. Nordheim, Zur Elektronentheorie der Metalle. I, Ann. Phys. 9 (1931) 607.
[36] J.O. Linde, An experimental study of the resistivity-concentration dependence of alloys, Helv. Phys. Acta 41 (1968) 1007–1015.
[37] C.J. Kuehmann, P.W. Voorhees, Ostwald ripening in ternary alloys, Metall. Mater. Trans. A 27 (1996) 937–943, https://doi.org/10.1007/BF02649761
[38] S. Semboshi, H. Tsuda, Y. Kanano, A. Iwase, T. Takasugi, Thermal conductivity of Ni3V– Ni3Al pseudo-binary alloys, Intermetallics, 59, 2015, pp. 1–7. Htts://doi.org/10.1016/j.intermet.2014.12.006.
[39] H. Numakura, T. Ikeda, H. Nakajima, M. Koiwa, Diffusion in Ni_3Al, Ni_3Ga and Ni_3Ge, Mater. Sci. Eng. A 312 (2001) 109–117, https://doi.org/10.1016/S0921-5093(00)01864-5
[40] B. Chanda, G. Potnis, P.P. Jana, J. Das, A review on nano-/ultrafine advanced eutectic alloys, J. Alloy. Compd. 827 (2020) 154226, https://doi.org/10.1016/j.jallcom.2020.154226